Laboratory Observations of Electron Heating and Non-Maxwellian Distributions at the Kinetic Scale during Electron-Only Magnetic Reconnection

Peiyun Shi, Prabhakar Srivastav, M. Hasan Barbhuiya, Paul A. Cassak, Earl E. Scime, and M. Swisdak

Phys. Rev. Lett. **128**, 025002 — Published 11 January 2022

DOI: 10.1103/PhysRevLett.128.025002

Laboratory Observations of Electron Heating and non-Maxwellian Distributions at the Kinetic Scale During Electron-Only Magnetic Reconnection

Peiyun Shi,[1,*] Prabhakar Srivastav,[1] M. Hasan Barbhuiya,[1] Paul A. Cassak,[1] Earl E. Scime,[1,†] and M. Swisdak[2]

[1]*Department of Physics and Astronomy and the Center for KINETIC Plasma Physics, West Virginia University, Morgantown, West Virginia 26506, USA*

[2]*Institute for Research in Electronics and Applied Physics, University of Maryland, College Park, Maryland 20742, USA*

(Dated: December 8, 2021)

Non-Maxwellian electron velocity distribution functions comprised of a warm bulk population and a cold beam are directly measured during electron-only reconnection with a strong out-of-plane (guide) magnetic field in a laboratory plasma. Electron heating is localized to the separatrix and the electron temperature increases continuously along the separatrix. The measured gain in enthalpy flux is 70% of the incoming Poynting flux. The electron beams are oppositely directed on either side of the X-point and their velocities are comparable to, and scale with, the electron Alfvén speed. Particle-in-cell simulations are consistent with the measurements. The experimental results are consistent with, and go beyond, recent observations in the magnetosheath.

Magnetic reconnection is a ubiquitous process that converts magnetic energy into thermal and kinetic energy of a plasma through the change of magnetic topology [1]. Although reconnection is responsible for various explosive phenomena at macroscopic scales, such as coronal mass ejections [2], geomagnetic storms [3], relativistic jets [4] and sawtooth oscillations in fusion plasmas [5–8], it is governed by processes at the microscopic, kinetic (the gyroradii of ions and electrons), scale [9]. Satellite missions [10–12] and simulations [13] have provided details of electron and ion velocity distribution functions (EVDFs and IVDFs) at the kinetic scale that have led to important insights into the physics of reconnection.

Recently, Phan *et al.* [14] reported satellite observations of electron-only reconnection in Earth's magnetosheath downstream of a quasi-parallel bow shock, where Alfvénic electron jets in opposite directions on either side of an X-point provided a "smoking-gun" signature of reconnection. Throughout the spacecraft trajectory through the magnetosheath, no Alfvénic ion jets associated with reconnection were observed. It was demonstrated in two-dimensional (2D) particle-in-cell (PIC) simulations that ions start to decouple from the reconnection process when the island-to-island system size Δ decreases below 40 times the ion kinetic scale [15]. The reconnection rate and electron outflow speed are significantly higher in 2D electron-only reconnection than in ion-coupled reconnection [15] and can be even higher in 3D [16]. Electron-only reconnection is thought to be important during the cascade of energy to kinetic scales in magnetized plasma turbulence [17–21] and near collisonless shocks [22–24]. However, less is known about how energy conversion during electron-only reconnection differs from fully ion-coupled reconnection, which can be very different at electron scales than ion scales [25, 26]. Half the available magnetic energy was measured to be converted into bulk electron kinetic energy and the other half was inferred to be converted into electron thermal energy, but no direct measurement of electron heating was possible in the Phan *et al*. observations [14]. No systematic observational or numerical study of heating in electron-only reconnection has been carried out to date.

Bulk electron and ion heating at the kinetic scale have been reported in laboratory reconnection studies [27–29] through electrostatic probe [30] and spectroscopic [31] measurements that do not resolve EVDFs. Indirect [32, 33] and ex-situ [34, 35] EVDF measurements have been reported in high-energy-density reconnection experiments. Fusion and heliospheric-relevant laboratory reconnection experiments have heretofore not directly measured VDFs at kinetic scales [36–38].

In this letter, we present experimental measurements of electron heating and energization in a laboratory study of electron-only reconnection with normalized plasma parameters comparable to those of the magnetosheath event [14]. Unique to the present study is that direct measurements of EVDFs at electron kinetic scales are obtained in the PHAse Space MApping (PHASMA) device [39, 40]. Incoherent Thomson scattering (TS) [41] provides non-perturbative, localized, direct EVDF measurements with sub-mm spatial resolution (1/3 of the electron inertial length) and 10 ns temporal resolution (1/10 the transit time of the electron fluid through the electron diffusion region). The electron temperature T_e found from the EVDFs implies the measured gain in electron enthalpy flux is up to 70% of the incoming Poynting flux. In a first for a laboratory reconnection experiment, non-Maxwellian EVDFs with oppositely directed jet-like flow features are observed on either side of the X-point. The flows are $0.6-1$ times the expected outflow speed, the electron Alfvén speed V_{Ae} based on the reconnecting magnetic field strength B_{recx}. We conclude that these flows are signatures of bulk electron acceleration resulting from reconnection. The results are compared to 2D PIC simulations and the electron thermal energy gains are comparable to those in the experiment. We further compare our results to previous observations and experiments that inferred the energy partition during reconnection. Our measurements provide confirmation that a significantly higher fraction of incoming energy goes to electrons during electron-only reconnection.

The experimental configuration for the reconnection study is similar to previous linear reconnection devices [42–44] and is shown in Fig. 1(a). Two 1-m long flux ropes (blue) are

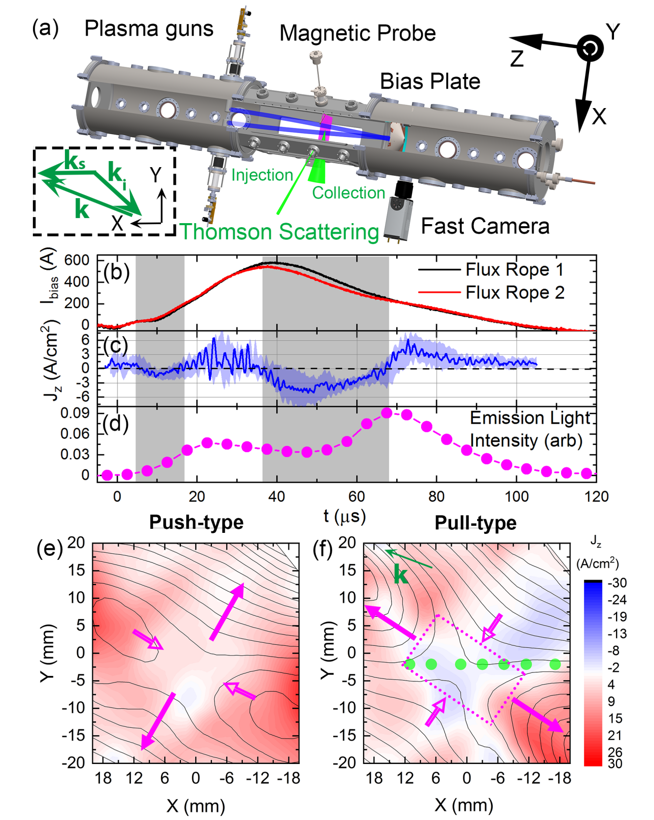

FIG. 1. (a) The PHASMA experiment. Green arrows in the dashed box show the incident $\vec{k}_i$ and scattered $\vec{k}_s$ wavevectors of TS; (b) Bias current versus time for the two flux ropes; (c) Axial current density near the X-point with the error bars given by the color band; (d) Emission light intensity recorded by the fast camera downstream of the bias plate; (e,f) Reconnecting magnetic field topology (black lines) and axial current density (colors) at $t = 15$ μs and 47 μs. Green dots indicate locations of TS measurements. Magenta arrows denote inflows (shorter open) and outflows (longer solid), suggesting push-type (e) and pull-type (f) reconnection. The dotted rectangle is used to calculate energy fluxes.

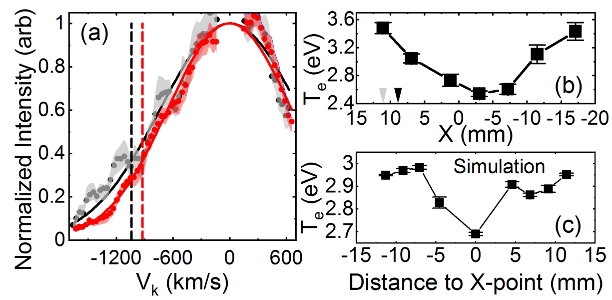

FIG. 2. (a) EVDFs at $x = 7$ mm (black circles) and $x = 1$ mm (red circles). The color bands show the measurement deviation. Solid lines are Maxwellian fits while the vertical dashed lines are the thermal speeds of each fit. (b) T_e at the green dots in Fig. 1(f) at $t = 47$ μs. The black arrow is 1.8 δ from the X-point where the enthalpy increase is calculated. The gray arrow is the location used for testing the scaling of electron enthalpy increase with B_{recx}. (c) The variance of T_e along the separatrix obtained from a 2D PIC simulation

created by two plasma guns (left side) separated by a distance $\Delta = 60$ mm along x. An argon plasma is drawn out of the guns with a bias potential applied between the gun and a conical anode (right side). The conical anode has a hole at its apex for diagnostic access. The two flux ropes interact, resulting in reconnection [45].

The bias currents I_{bias} of the flux ropes versus time are plotted in Fig. 1(b). In contrast to previous experiments, the peak $I_{bias} = 500$ A is larger than the threshold current of the $m = 1$ kink [39]. The larger bias currents increase the magnetic energy available for reconnection. The discharges are kept kink-free with excellent shot-to-shot repeatability by shortening the pulse duration so it is comparable to or even shorter than the axial Alfvén time of 50 μs. Thus, reconnection ends well before the kink can grow.

The magnetic field $\mathbf{B}_\perp$ perpendicular to the axial (guide) field B_g is measured by scanning one magnetic probe array over many reproducible discharges [45, 46], yielding $B_{recx} =$ 15 G and $B_g = 375$ G. The axial current density J_z is derived from $\nabla \times \mathbf{B}_\perp/\mu_0$, which is plotted around $(x, y) = (3, -5)$ mm as a function of time in Fig. 1(c). J_z reverses direction during two time periods, highlighted with gray shading in Fig. 1(b,c,d), during when J_z is opposite to the direction of the axial current of the flux ropes, a signature of reconnection between the flux ropes [42]. The current sheet thickness $\delta \approx 3\ d_e$, or $0.1\rho_s$, where $\rho_s = C_s/\omega_{ci}$ is the ion gyroradius based on the ion sound speed $C_s = [\gamma k_B(T_e + T_i)/m_i]^{1/2}$, $\gamma = 5/3$ is the ratio of specific heats, k_B is Boltzmann's constant, T_i is the ion temperatures, m_i is the ion mass, and ω_{ci} is the ion gyrofrequency based on the total magnetic field B. The duration of reconnection is around 20 μs, equivalent to about 200 τ, where the transit time $\tau \sim \delta/V_{in} \simeq 0.1$ μs, and the inflow speed $V_{in} \sim 0.1\ V_{Ae}$, suggesting that steady-state reconnection is likely achieved. Two intervals of increasing emission light intensity recorded by a fast camera in Fig. 1(d) follow the two reconnection periods. Bursts of increased emission do not appear during single flux rope experiments.

Figure 1(e,f), shows the projections of magnetic field lines on the xy plane, overplotted on a 2D plot of J_z. These plots show a classic X-type topology of reconnection. During the early phase of the plasma pulse ($t \sim 15$ μs, panel (e)), push-type reconnection occurs when the two flux ropes approach each other, as identified by the evolution of $\mathbf{B}_\perp$. The inflow and outflow are represented by the shorter open arrows and longer solid arrows, respectively. Pull-type reconnection [47] occurs later ($t \simeq 47$ μs, panel (f)) as the two flux ropes move apart. The reversed current in the inflow region, with different spatial profiles and temporal evolution than that around the X-point, is associated with eddy currents associated with single flux ropes [48].

The plasma parameters for this experiment are summarized in the Supplement. We include analogous parameters for the magnetosheath electron-only reconnection event [14]. Here, $\rho_s \gg d_e$, a well-studied parameter regime in fusion and the heliosphere [8]. The system size Δ is roughly 1.5 ρ_s, much

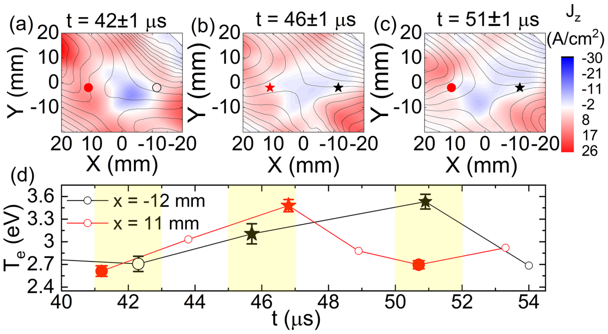

FIG. 3. (a-c) Reconnecting magnetic field topology (black lines) and axial current density (colors) at $t = 42 \pm 1$ μs, 46 ± 1 μs and 51 ± 1 μs. Solid circles, blank circles and solid stars denote the outflow, inflow and separatrix regions, respectively. (d) T_e measurements at $x = 11$ mm (red) and $x =$ -12 mm (black) as a function of time. Yellow shaded rectangles denote times corresponding to (a-c).

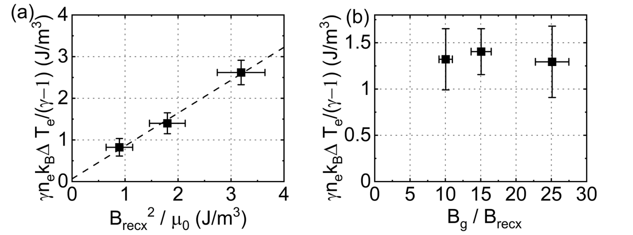

FIG. 4. Measured electron enthalpy density increase $[\gamma/(\gamma-1)]n_e k_B \Delta T_e$ versus (a) reconnecting magnetic enthalpy B_{recx}^2/μ_0 and (b) ratio of guide field to reconnecting field B_g/B_{recx}.

less than the 40 ρ_s scale necessary for the ions to fully couple to the reconnection [15]. Moreover, the time scale of 20 μs over which reconnection occurs is far smaller than the ion cyclotron time $\tau_{ci} = 2\pi/\omega_{ci} \sim 70$ μs, so the reconnection is electron-only. The mean free path for electron-ion collisions is about 13 mm ($\sim 2\ \delta$) and the electron-ion collision time is 0.02 μs ($\sim 0.2\ \tau$), so individual electrons transiting the current sheet experience few collisions, i.e., the plasma is marginally collisional at most.

The electron temperature is obtained directly from EVDFs using the TS diagnostic as shown in Fig. 1(a). The EVDFs are measured along $\vec{k}$. The spatial resolution is 0.5 mm, sufficient to measure EVDFs at and below the electron inertial scale $d_e = c/\sqrt{n_e e^2/m_e \varepsilon_0} \approx 1.7$ mm, where e and m_e are the electron charge and mass, and electron density $n_e = 1 \times 10^{19}$ m^{-3}. Spatial scanning of the EVDF measurements is achieved by translating the plasma guns along x. EVDFs at $x = 7$ mm and $x = 1$ mm at $t = 47$ μs are plotted as black and red circles in Fig. 2(a). Each EVDF is an average of 40 laser shots at the same time in the discharge. The solid lines are Maxwellian fits to the EVDFs and the vertical dashed lines denote the thermal speeds v_{Te} obtained from the fits. The relative uncertainty of T_e measurements is $< 10\%$ (see the Supplement), so that the sub-eV changes observed in T_e during reconnection are statistically significant.

One entire separatrix is accessible by translating the plasma guns along x at $t = 47$ μs, shown by the green dots in Fig. 1(f). This allows us to investigate the spatial temperature profile in the region where heating is expected to be most prominent [49]. Figure 2(b) shows the electron temperature T_e as a function of x for these points. It increases from 2.6 eV around the X-point at $x = 0$ mm to 3.4 eV downstream of the separatrix in either direction, an increase of nearly 30%.

Due to the natural rotation of the reconnection geometry as the flux ropes rotate, we measure EVDFs in different regions, including the separatrix, inflow and outflow regions, by firing the TS diagnostic at different times. Figure 3(a-c) shows field line projections and axial current density at $t = 42 \pm 1$ μs, 46 ± 1 μs and 51 ± 1 μs, respectively. The $x = 11$ mm measurement, shown in red, is in the outflow region (solid circles in panels (a) and (c)) at $t = 41$ μs and 51 μs, and the separatrix region (solid star in panel (b)) at $t = 47$ μs. The $x = -12$ mm measurement begins in the inflow region (black open circle in panel (a)) at $t = 42$ μs and moves to the separatrix region (black solid stars in panels (b) and (c)) at $t = 46$ μs and 51 μs.

The corresponding temporal evolution of T_e obtained from measured EVDFs at these two points is shown in Fig. 3(d). The time ranges plotted in panels (a)-(c) are highlighted with yellow bands. The points during this period corresponding to those in the inflow and outflow regions reveal lower temperatures, while the points corresponding to the separatrices are sites of significant electron heating. This localized heating around separatrices is consistent with previous work on reconnection with a finite B_g [26, 49].

The electron heating ΔT_e is evaluated by comparing the local electron temperature T_e to the value in the inflow region [50]. From Fig. 3(d), we find $T_e = 2.7 \pm 0.1$ eV in the inflow region and it peaks at $T_e = 3.5 \pm 0.1$ eV around the separatrix. The measured electron temperature of $T_e = 3.0 \pm 0.1$ eV at $1.8\ \delta = 9$ mm downstream of the X-point is chosen to directly compare to the magnetosheath observations [14]. To compare to previous work on the energy partition, the ratio of the electron enthalpy flux at this location to the incoming Poynting flux is $[\gamma/(\gamma-1)]n_e k_B \Delta T_e/(B_{recx}^2/\mu_0) = 70\%$. We assume the system is adiabatic because B_g is large and the distributions are close to Maxwellian.

To investigate the relative importance of collisions in the conversion of magnetic to thermal energy, we consider the rectangle of thickness $2\ \delta = 10$ mm and length $2\ L = 20$ mm around the X-point, the dotted rectangle in Fig 1(f). The collisional Ohmic heating power per unit length out of the reconnection plane is estimated as $P_{Ohmic} = \eta J_z^2 (2\delta \cdot 2L) \sim 0.03$ kW/m, where the Spitzer resistivity η is used and J_z near the X-point is used throughout the rectangle for simplicity. We compare this to the rate of electron enthalpy production per unit length in the out-of-plane direction, ΔH. We roughly estimate its magnitude based on local ΔT_e values, as our T_e measurements are limited to a single separatrix and the heating on opposite separatrices is different in guide field reconnection [49]. Using the measured value 1.8 δ downstream for ΔT_e, we find $\Delta H = [\gamma/(\gamma-1)]n_e k_B \Delta T_e (2\delta \cdot 2L)/\tau \sim 2$ kW/m. The

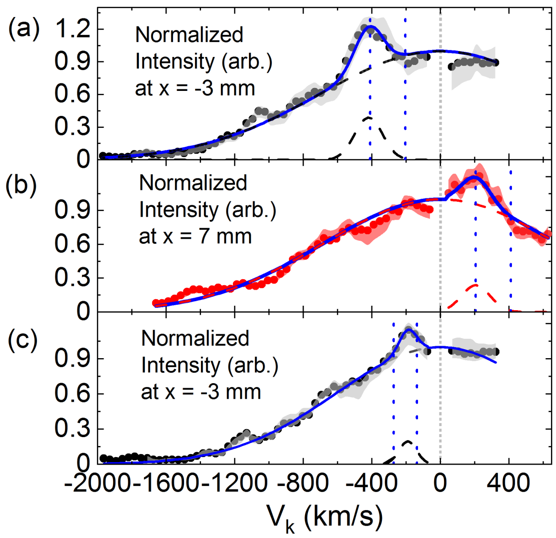

FIG. 5. EVDFs for the $B_{recx} = 15$ G discharge showing oppositely directed beams on either side of the X-point. (a) $x = -3$ mm (black circles) and (b) $x = 7$ mm (red circles). Dashed lines are Maxwellian fits for the bulk and beam and the solid line is their sum. The dotted vertical lines denote speeds of $V_{Ae}/2$ and V_{Ae}. (c) EVDF measured at $x = -3$ mm for the $B_{recx} = 10$ G discharge.

two-orders of magnitude difference between P_{Ohmic} and ΔH suggests that, even allowing for possible underestimation of J_z and the use of the Spitzer prediction for η for a marginally collisional plasma, Ohmic heating is not the dominant process for magnetic to thermal energy conversion and that other kinetic-scale processes must be responsible for the energy conversion. Note the rate of magnetic enthalpy deposition per unit length in the out-of-plane direction $(B_{recx}^2/\mu_0)\cdot(2V_{in}\cdot 2L) = 3$ kW/m is large enough to account for the observed electron heating.

To confirm that the released magnetic energy drives the electron heating, we vary B_{recx} from 10 to 20 G. Figure 4(a) shows the electron enthalpy density increase $[\gamma/(\gamma-1)]n_e k_B \Delta T_e$ a distance 1.8 δ from the X-point as a function of the reconnecting magnetic enthalpy density B_{recx}^2/μ_0. The dependence is linear, as expected if reconnection causes the heating [50], with a fitted slope of 0.8 (dashed line). Figure 4(b) shows the change in electron enthalpy density versus the ratio of guide field to reconnecting field B_g/B_{recx} in the range of 10-25. Since the reconnection rate is largely independent of guide field [51, 52], the lack of dependence of electron heating on guide field is expected. This result is reproduced in our simulations (see the Supplement).

During reconnection, we observe non-Maxwellian EVDFs with oppositely directed beams on either side of the X-point. Figure 5(a) shows the EVDF as a function of V_k, the velocity component along $\vec{k}$, at $x = -3$ mm and $t = 55$ µs. $\vec{k}$ is at an angle of 22.5°, as shown in Fig. 1(a,f), and is mostly in the outflow direction. There is a clear beam feature with a negative velocity. A composite fit, shown as the solid line, based on two Maxwellian EVDFs shown individually as dashed lines, reveals that the total EVDF is expressible as a combination of a nearly stationary, warm bulk electron population and a colder, much less dense, electron beam at a velocity of $V_k \simeq$ -440 km/s. The speed of the feature is close to $V_{Ae} = 430$ km/s. The electron beam has a relative density of roughly $n_e^b \approx 0.04 n_e$ and an electron temperature of $T_e^b \approx 0.02\,\mathrm{eV} = 0.01 T_e$.

Figure 5(b) shows the EVDF on the other side of the X-point at $x = 7$ mm. The EVDF also exhibits a beam feature but with $V_k > 0$. A fit to two Maxwellian distributions yields a flow feature speed of $V_k = +210$ km/s (half of V_{Ae}). To investigate if this feature is a reconnection outflow jet, we show the EVDF from an experiment in which B_{recx} is reduced from 15 G to 10 G in Fig. 5(c). The speed of the beam at the same location as Fig. 5(a) drops to -180 km/s as V_{Ae} drops to 280 km/s. Thus, we measure oppositely directed electron beams at speeds $(0.6-1)V_{Ae}$ near the X-point, which is strong evidence of bulk electron acceleration [14]. Further from the X-point, the outflow appears to be decelerated, possibly by closed field lines of the flux ropes or collisions.

We compare the experimental results to 2D simulations using the collisionless PIC code p3d [53] (see the Supplement for details) with a true electron to argon ion mass ratio, the same island separation Δ, and $B_g/B_{recx} = 25$. In the simulation, the heating happens in a narrow region of thickness $\simeq 1$ mm $\simeq 0.6\ d_e \simeq 7\ \rho_e$ and the heating increases with distance from the X-point in excellent qualitative and reasonable quantitative agreement with the experiment. Relative to the temperature in the upstream region, ΔT_e is up to 0.55 eV (see Fig. 2(c)), comparable to the experimental result of 0.8 eV. Interestingly, the simulations do not reproduce the measured EVDFs, suggesting the cause is manifestly 3D.

In an experimental study with finite B_g and $\Delta \simeq 5\ \rho_s$, Fox *et al.* [26] reported a similar electron heating structure, but the ratio of electron enthalpy flux to Poynting flux was much smaller, about 23% at 1.8 δ away from the X-point. Our measured ratio of 70% is also considerably larger than the 14% reported by Yamada et al. [28] for zero guide field reconnection. Thus, as expected [25], the conversion of energy at electron scales is different than in ion coupled reconnection.

In the magnetosheath electron-only reconnection study [14], 50% of the incoming B_{recx}^2/μ_0 appeared as kinetic energy. The other 50% was assumed to appear as thermal energy because the associated temperature increase was too small to measure. The increase in T_e in PHASMA is directly measured. We also note the satellite observations of electron jets were based on asymmetries in the EVDFs at large velocities because instrumental effects prevented measurements at velocities comparable to V_{Ae}. In other magnetosheath studies in which electron velocities comparable to V_{Ae} are resolvable, a well-defined, cold, electron beam moving in the outflow direction (reminiscent of the EVDFs observed in this experiment) is observed superimposed on a background electron population close to the separatrix [54].

We acknowledge fruitful discussions with Wondwossen Eshetu, Benoit Lavraud, Tai Phan, Prayash Sharma Pyakurel, and Shan Wang. This work was supported by awards NSF

AGS 1602769 and PHY 1804428, 1827325 and 1902111, NASA 80NSSC19M0146, and DoE DE-SC0020294. This research uses resources of NERSC, a DOE Office of Science User Facility supported by the Office of Science under Contract no. DE-AC02-05CH11231.

* peiyun.shi@mail.wvu.edu
† earl.scime@mail.wvu.edu

[1] M. Yamada, R. Kulsrud, and H. Ji, Reviews of Modern Physics **82**, 603 (2010).
[2] T. G. Forbes, Journal of Geophysical Research: Space Physics **105**, 23153 (2000).
[3] J. Dungey, Physical Review Letters **6**, 47 (1961).
[4] E. M. de Gouveia Dal Pino, P. P. Piovezan, and L. H. S. Kadowaki, Astronomy & Astrophysics **518**, A5 (2010).
[5] S. von Goeler, W. Stodiek, and N. Sauthoff, Physical Review Letters **33**, 1201 (1974).
[6] A. W. Edwards, *et al.*, Physical Review Letters **57**, 210 (1986).
[7] E. Scime, S. Hokin, N. Mattor, and C. Watts, Physical Review Letters **68**, 2165 (1992).
[8] M. Yamada, F. M. Levinton, N. Pomphrey, R. Budny, J. Manickam, and Y. Nagayama, Physics of Plasmas **1**, 3269 (1994).
[9] E. G. Zweibel and M. Yamada, Annual Review of Astronomy and Astrophysics **47**, 291 (2009).
[10] C. P. Escoubet, M. Fehringer, and M. Goldstein, Annales Geophysicae **19**, 1197 (2001).
[11] V. Angelopoulos, in *The THEMIS Mission*, edited by J. L. Burch and V. Angelopoulos (Springer, New York, NY., 2009).
[12] J. L. Burch, T. E. Moore, R. B. Torbert, and B. L. Giles, Space Science Reviews **199**, 5 (2016).
[13] M. Hesse, T. Neukirch, K. Schindler, M. Kuznetsova, and S. Zenitani, Space Science Reviews **160**, 3 (2011).
[14] T. D. Phan, *et al.*, Nature **557**, 202 (2018).
[15] P. Sharma Pyakurel, *et al.*, Physics of Plasmas **26**, 82307 (2019).
[16] P. S. Pyakurel, M. A. Shay, J. F. Drake, T. D. Phan, P. A. Cassak, and J. L. Verniero, Phys. Rev. Lett. **127**, 155101 (2021).
[17] J. E. Stawarz, *et al.*, The Astrophysical Journal Letters **877**, L37 (2019).
[18] F. Califano, S. S. Cerri, M. Faganello, D. Laveder, M. Sisti, and M. W. Kunz, Frontiers in Physics **8**, 317 (2020).
[19] C. Vega, V. Roytershteyn, G. L. Delzanno, and S. Boldyrev, The Astrophysical Journal Letters **893**, L10 (2020).
[20] G. Arró, F. Califano, and G. Lapenta, Astronomy & Astrophysics **642**, A45 (2020).
[21] N. F. Loureiro and S. Boldyrev, The Astrophysical Journal **890**, 55 (2020).
[22] I. Gingell, *et al.*, Geophysical Research Letters **46**, 1177 (2019).
[23] N. Bessho, L.-J. Chen, S. Wang, M. Hesse, and L. B. Wilson III, Geophysical Research Letters **46**, 9352 (2019).
[24] N. Bessho, L.-J. Chen, S. Wang, M. Hesse, L. B. Wilson, and J. Ng, Physics of Plasmas **27**, 092901 (2020).
[25] J. P. Eastwood, *et al.*, Physical Review Letters **125**, 265102 (2020).
[26] W. Fox, F. Sciortino, A. v. Stechow, J. Jara-Almonte, J. Yoo, H. Ji, and M. Yamada, Physical Review Letters **118**, 125002 (2017).
[27] Y. Ono, *et al.*, Plasma Physics and Controlled Fusion **54**, 124039 (2012).
[28] M. Yamada, J. Yoo, J. Jara-Almonte, H. Ji, R. M. Kulsrud, and C. E. Myers, Nature Communications **5**, 4774 (2014).
[29] H. Tanabe, *et al.*, Physical Review Letters **115**, 215004 (2015).
[30] W. Fox, M. Porkolab, J. Egedal, N. Katz, and A. Le, Physical Review Letters **101**, 255003 (2008).
[31] M. R. Brown, Physics of Plasmas **6**, 1717 (1999).
[32] J. D. Hare, *et al.*, Physical Review Letters **118**, 085001 (2017).
[33] A. L. Milder, J. Katz, R. Boni, J. P. Palastro, M. Sherlock, W. Rozmus, and D. H. Froula, Physics of Plasmas **28**, 82102 (2021).
[34] A. E. Raymond, *et al.*, Phys. Rev. E **98**, 043207 (2018).
[35] J. Y. Zhong, *et al.*, The Astrophysical Journal: Supplement Series **225**, 30 (2016).
[36] G. G. Howes, Physics of Plasmas **25**, 055501 (2018).
[37] Y. Liu, P. Shi, X. Zhang, J. Lei, and W. Ding, Review of Scientific Instruments **92**, 71101 (2021).
[38] H. M. Milchberg and E. E. Scime, arXiv e-prints , arXiv:1910.09084 (2019).
[39] P. Shi, *et al.*, Physics of Plasmas **28**, 32101 (2021).
[40] E. E. Scime, *et al.*, in *2021 International Conference on Electromagnetics in Advanced Applications (ICEAA)* (2021) pp. 014–014.
[41] P. Shi, P. Srivastav, C. Beatty, R. S. Nirwan, and E. E. Scime, Review of Scientific Instruments **92**, 33102 (2021).
[42] T. P. Intrator, X. Sun, G. Lapenta, L. Dorf, and I. Furno, Nature Physics **5**, 521 (2009).
[43] R. L. Stenzel and W. Gekelman, Physical Review Letters **42**, 1055 (1979).
[44] P. Shi, K. Huang, Q. Lu, and X. Sun, Plasma Physics and Controlled Fusion **61**, 125010 (2019).
[45] X. Sun, T. P. Intrator, L. Dorf, J. Sears, I. Furno, and G. Lapenta, Physical Review Letters **105**, 255001 (2010).
[46] W. Gekelman, T. De Haas, W. Daughton, B. Van Compernolle, T. Intrator, and S. Vincena, Physical Review Letters **116**, 235101 (2016).
[47] M. Yamada, H. Ji, S. Hsu, T. Carter, R. Kulsrud, N. Bretz, F. Jobes, Y. Ono, and F. Perkins, Physics of Plasmas **4**, 1936 (1997).
[48] J. von der Linden, J. Sears, T. Intrator, and S. You, Physical Review Letters **121**, 35001 (2018).
[49] R. G. Kleva, J. F. Drake, and F. L. Waelbroeck, Physics of Plasmas **2**, 23 (1995).
[50] M. A. Shay, C. C. Haggerty, T. D. Phan, J. F. Drake, P. A. Cassak, P. Wu, M. Oieroset, M. Swisdak, and K. Malakit, Physics of Plasmas **21**, 122902 (2014).
[51] M. Hesse, K. Schindler, J. Birn, and M. Kuznetsova, Physics of Plasmas **6**, 1781 (1999).
[52] P. L. Pritchett, Journal of Geophysical Research: Space Physics **106**, 3783 (2001).
[53] A. Zeiler, D. Biskamp, J. Drake, B. Rogers, M. Shay, and M. Scholer, Journal of Geophysical Research: Space Physics **107**, 3783 (2002).
[54] S.-C. Bai, Q. Shi, Q.-G. Zong, X. Wang, A. Tian, A. W. Degeling, C. Yue, I. J. Rae, Z.-Y. Pu, and S. Fu, Journal of Geophysical Research: Space Physics **124**, 7494 (2019).